A fluorescent and colorimetric sensor based on a porphyrin doped polystyrene nanoporous fiber membrane for HCl gas detection†

Min Hu, [ID] [a] Weimin Kang,*[ab] Yixia Zhao,[b] Jie Shi[a] and Bowen Cheng [ID] *[ab]

A facile fluorescent and colorimetric sensor capable of naked-eye detection of gaseous hydrogen chloride (HCl) was developed. This technology uses the optical probe 5,10,15,20-tetraphenylporphyrin immobilized in a polystyrene nanoporous fiber membrane ($TPPH_2$-PS NFM) which was fabricated by electrospinning. The surface morphology and porous structures of the $TPPH_2$-PS NFM were characterized and HCl gas sensing properties of the sensor was monitored by fluorescence spectrophotometry. Exposure to HCl gas causes apparent color change of the sensor from pink to yellow-green. The sample of THF-40 showed the maximum pseudo-second-order rate constant due to its largest specific surface area and pore volume. The detection limit was found to be 46 ppb and the response time was 5 s. The sensor exhibits excellent reversibility and prompt response and recovery which shed light on developing low-cost HCl gas sensing systems.

Introduction

Fluorescent and colorimetric sensors have emerged as a powerful new approach toward the detection of gaseous pollutants at ppm or ppb concentration levels.[1–4] In contrast to other detecting approaches, fluorescent and colorimetric sensors present a number of advantages, such as instrumental simplicity, low-cost, high sensitivity, fast response, good reversibility, permit real-time analyses, *etc.*[5] Monitoring of gaseous pollutants is very important because the quality of the atmospheric environment is directly relevant for human health and life. HCl gas is one of the toxic gases which is mainly derived from complete burning of halogenated polymers, incineration of plants and absorbing towers of semiconductor factories and is strictly regulated in many countries now.[6–8] The threshold for tolerably safe exposure to HCl gas is 10 ppm and the exposure limit of 5 ppm has been identified as a work place hazard.[9,10] For this reason, a reliably fluorescent and colorimetric sensor for HCl gas detection is strongly demanded.

Hitherto, the centerpiece of most fluorescent and colorimetric sensors is the fluorescent sensing materials.[11–13] Porphyrin is a common organic dye and has attracted much interest as the fluorescent sensing materials for toxic gas detection due to its highly conjugated π-electron structure, distinctive fluorescence bands in the visible region as well as selectivity of the designated gas.[14–16] Most of these porphyrin-based optochemical sensors mainly incorporate porphyrin into glasses, sol–gel, solid state films, *etc.*[17–22] It is well known that the efficiency of these gas sensor is greatly dependent on the structure of the sensing materials.[11] Due to its large specific surface area, high porosity and excellent accessibility for gaseous analytes, porous structure is highly attractive to the sensing materials. For example, F. W. Lin *et al.*[23] fabricated honeycomb-patterned porous films for sensing of hazardous HCl gas. The well-ordered porous films sensor shows remarkable fluorescence quenching behavior toward HCl gas with quenching ratios of 72% higher than that of the corresponding dense film. Y.-Y. Lv *et al.*[24] prepared a nanofibrous membrane of porphyrinated polyimide for the rapid detection of HCl gas. The fluorescence quenching of nanofibrous membrane is much significant than that of dense film due to its three dimensional and porous structures, and hence good gas accessibility.

Recently, electrospinning is one of the most promising approaches to fabricate nanofibers with nano- and micro-porous structure.[25–27] Polystyrene (PS), a common thermoplastic polymer with low surface energy, has been widely used to fabricate porous nanofibers *via* directly electrospinning method.[28,29] Owing to its low toxicity, cheaper cost and excellent photostability, PS has become the most popular smart material to envelop sensitive probes for oxygen measurement.[30] However, to the best of our knowledge, there have been few studies regarding PS nanoporous fibers for the detection of HCl gas.[13,31–33]

In this work, we successfully demonstrated that $TPPH_2$-PS NFM can be used for the naked-eye detection of HCl gas at ppm-

[a] School of Textile, Tianjin Polytechnic University, Tianjin 300387, PR China. E-mail: kweimin@126.com; bowen15@tjpu.edu.cn

[b] Key Laboratory of Separation Membranes and Membrane Processes, Tianjin 300387, PR China

level based on a simple color change. The PS nanoporous fiber membrane was prepared by electrospinning and $TPPH_2$ was immobilized in the PS NFM uniformly. Furthermore, HCl gas sensing properties of the $TPPH_2$-PS NFM sensor was monitored *via* distinct fluorescence variation.

Experimental

Materials

Polystyrene (PS) with molecular weight of $M_w = 208\,000$ g mol^{-1} was provided by Wako, Japan. 5,10,15,20-Tetraphenylporphyrin ($TPPH_2$) (reagent grade, 97%) was purchased from J&K Technology Co., China. Tetrahydrofuran (THF) and *N,N*-dimethylformamide (DMF) were obtained from Tianjin Fengchuan Chemical Reagent Co., Ltd., China.

Preparation of the $TPPH_2$-PS NFM

PS and $TPPH_2$ were dissolved in THF : DMF mixtures to obtain the electrospinning solutions. The concentration of PS, $TPPH_2$ contents and weight ratios of THF : DMF mixtures were listed in Table 1. All the chemical reagents were used without further purification. Then the spinning solution was placed in a syringe and was pumped through a metal capillary with an inner diameter of 0.8 mm by a syringe pump (WZL-506, Smiths Medical Instrument Zhejiang Co., Ltd., China). The solution feeding rate was controlled at 1.0 mL h^{-1}. A high voltage power supply (DW-P303-1ACD8, Tianjin Dongwen High Voltage Co., China) was used to generate a potential difference of 20 kV between the capillary and an aluminum foil covered grounded metallic rotating roller rotated at 280 rpm. The work distance (WD) was kept at 20 cm. All the experiments were carried out at 25 °C and the relative humidity (RH) was 50 ± 2%. The spinning time was fixed in 5 h so that the thickness of $TPPH_2$-PS NFMs was 0.11 ± 0.005 mm. After electrospinning the $TPPH_2$-PS NFMs were dried in vacuum at 40 °C for 24 h.

Characterization

The morphology and cross-section of the electrospun $TPPH_2$-PS NFMs was observed by field emission scanning electron microscope (FE-SEM) (S-4800, Hitachi, Japan) at an acceleration voltage of 5 kV and high vacuum mode after gold coating. The average fiber diameter of each sample was measured by image analysis software (Image Pro Plus 6.0). Fluorescent images of the samples were captured on fluorescence microscope (Nikon A1$^+$, Nikon, Japan). The wavelength of excitation was 488 nm. N_2 adsorption–desorption data were measured using a specific surface and micropore analyzer (Autosorb-iQ, Quantachrome, USA). The specific surface area of the $TPPH_2$-PS NFM was obtained from the N_2 adsorption data in the relative pressure range from 0.05 to 0.3 by using the Brunauer–Emmett–Teller (BET) method. The total pore volume, pore size and its distribution of the fiber membrane were calculated by the Barrett–Joyner–Halenda (BJH) method. The thermogravimetric (TG) analysis was performed using a thermal analyzer (STA 409 PC/PG, Netzsch, Germany), under nitrogen flow, in a temperature range from 20 °C to 800 °C and at a heating rate of 10 °C min^{-1}. UV-vis absorbance spectra of the $TPPH_2$-PS NFMs were measured by UV-Visible spectrophotometer (EVOLUTION 220, Thermo, USA) which is assembly attached to the ISA-220 integrating sphere. The Czerny–Turner monochromator (Thermo, USA) was used and the acquisition time was 2 min. Fluorescence emission spectra were conducted on fluorescence spectrophotometer (F-380, Gangdong Sci., China) with a solid assembly to have excitation and emission at 45° to the membrane surface. Samples were excited at 420 nm and emission was measured at wavelength of 600–760 nm. Water contact angle measurements were performed with contact angle instrument (JYSP-180, Jinshengxin, China) using the static sessile drop method with DROP image advanced software to determine static contact angles.

HCl gas sensing setup

Sensor samples were prepared by cutting the $TPPH_2$-PS NFMs into round shape (the diameter is about 1 cm). HCl gas detection was carried out in a specially designed gas testing chamber comprising two high precision mass flow controllers (red-y, Voegtlin, Germany) which delivered a mixture of HCl gas and pure N_2 to obtain required HCl gas concentration. The volume of the gas testing chamber was 1 L. The HCl gas was detected at 40 °C in 50 ± 2% RH. The fluorescence intensity at 645 nm of the sensor (I_0 and I) before and after HCl gas exposure were recorded by the fluorescence spectrophotometer. After each exposure, the chamber was flushed with pure nitrogen to recover the $TPPH_2$-PS NFM until the fluorescence intensity at 645 nm of the sensor approximate the original I_0. Visible color variation of the sensor when exposed to HCl gas was recorded by a digital camera (IXUS 210, Canon, Japan) in the same condition to ensure the accuracy of these color pictures.

Results and discussion

Characterization of the $TPPH_2$-PS NFM

Fig. 1 shows the FE-SEM images of $TPPH_2$-PS NFMs from $TPPH_2$-PS solutions of various solvent compositions *via* electrospinning method. Nonporous and bead-on-string structure was obtained from only DMF solvent due to the high boiling point of DMF (153 °C) which was incompletely evaporated

Table 1 Formulas of the $TPPH_2$-PS electrospinning solutions

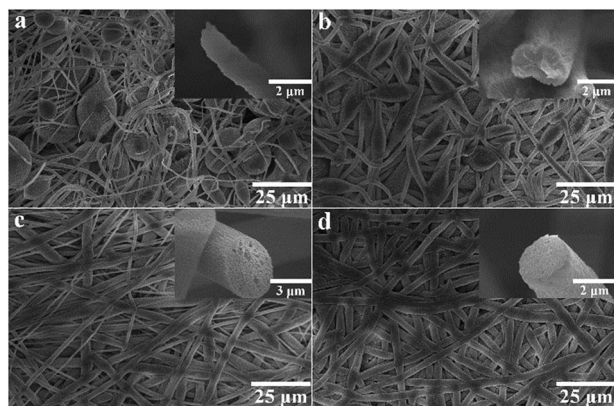| Sample	PS concentration (wt%)	$TPPH_2$ content (mg mL^{-1})	m(THF) : m(DMF)	$TPPH_2$/PS (g g^{-1})
THF-0	25	2.0	0 : 100	0.0063
THF-20	25	2.0	20 : 80	0.0064
THF-40	25	2.0	40 : 60	0.0067
THF-60	25	2.0	60 : 40	0.0066
$TPPH_2$-1.0	25	1.0	40 : 60	0.0033
$TPPH_2$-1.5	25	1.5	40 : 60	0.0050
$TPPH_2$-2.0	25	2.0	40 : 60	0.0067
$TPPH_2$-2.5	25	2.5	40 : 60	0.0083

Fig. 1 FE-SEM images of the TPPH$_2$-PS NFMs formed from various weight ratios of THF : DMF in solvent: (a) 0 : 100, (b) 20 : 80, (c) 40 : 60, (d) 60 : 40, respectively. The inset images were the cross-section of TPPH$_2$-PS fibers.

before the fibers were collected at the collector (Fig. 1a). With the increase of the low boiling point of THF (66 °C), the amount of bead-on-string structure decreased and disappeared when the ratio of THF was up to 40%. It can be seen that the fiber comprised a grooved sheath and a solid core when a solvent mixture with 20% THF was used (insets of Fig. 1b). With the increasing THF percentage in the solvent mixtures, the nanopores presented on the fiber surfaces, and the porous structure appeared to be throughout the cross-sections of these fibers (insets of Fig. 1c). As the THF content further increased, the 3D interconnected nanopores inside the fibers became more uniform and dense as shown in insets of Fig. 1d. The morphology of the TPPH$_2$-PS NFMs with different TPPH$_2$ content is shown in Fig. S1.† The TPPH$_2$ content has little impact on the fiber preparation and pore formation and the fiber diameter is in range of 800–3000 nm. Fluorescent images of the TPPH$_2$-PS NFM are shown in Fig. 2. Clearly, the TPPH$_2$-PS NF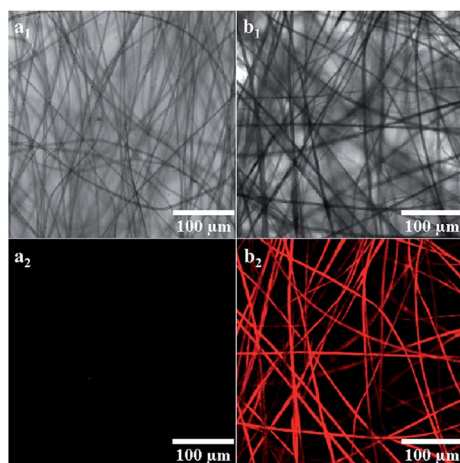M shows uniform red fluorescence, while the pure PS NFM without TPPH$_2$ doped shows none fluorescence. It confirms that TPPH$_2$ is homogeneously dispersed in the surface and inside of the nanoporous PS fiber membrane.

The main reasons for pores formation of the fibers have been proved to be the thermally-induced phase separation and vapor-induced phase separation by previous studies.[29,34] During electrospinning, the solvent evaporated from the polymer fluid jets involves the flash vaporization at the fiber surface and the diffusion from core to surface. In the meantime, moisture in the air will penetrate into the fluid jet while the solvent will diffuse out from the core of the jet. This is accompanied by cooling the fluid jets, leading to thermodynamically unstable jets and phase separation into polymer-rich and solvent-rich domains.[31] Eventually, the polymer-rich phase solidified into fiber matrix and the solvent-rich phase transformed into nanopores as the solvent diffused out. The difference in the porous structure of these fibers can be attributed to the competition between the rapid phase separation and solidification resulting from the mutual diffusion of the solvent within the jet and the surrounding moisture due to the different solvent compositions of THF and DMF utilized in electrospinning.

Fig. 3 presents the nitrogen adsorption–desorption isotherms and pore size distribution curves of the TPPH$_2$-PS NFMs formed with various ratios of THF–DMF. The isotherms of THF-0 and THF-20 are in accordance with the type III isotherm which is characteristic of macropores, while the isotherms of THF-40 and THF-60 are akin to a type II isotherm with a hysteresis loop which is the characteristics of mesopores and macropores according to the International Union and Applied Chemistry (IUPAC) classification.[34,35] The inset of Fig. 3 reveals that the pore size is in the range of 2–60 nm. Such porous structures are expected to contribute to higher specific surface area of these TPPH$_2$-PS NFMs. The specific surface area and pore volume derived from BET measurements as well as average fiber diameter of the TPPH$_2$-PS NFMs formed with various ratios of THF–DMF are show in Table 2. It is obvious that the varied solvent compositions exhibit the significant effects. THF-40 has the highest specific surface area of 58.63 m^2
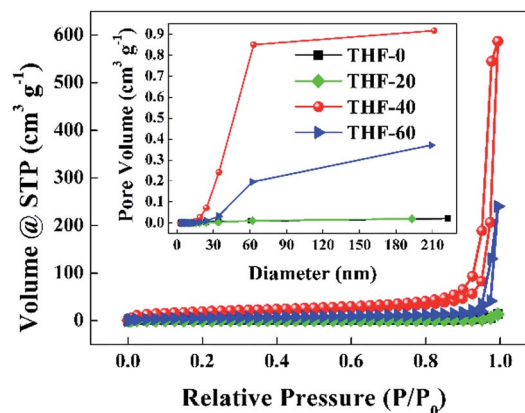

Fig. 2 Fluorescent images of the sample THF-40 with different TPPH$_2$ content: (a) 0 mg mL^{-1}, (b) 2.0 mg mL^{-1} (a$_1$, b$_1$-bright-field image, a$_2$, b$_2$-fluorescent image) (λ_{ex} = 488 nm).

Fig. 3 Nitrogen adsorption–desorption isotherms and pore size distribution curves (inset) of the TPPH$_2$-PS NFMs formed with various ratios of THF–DMF.

Table 2 The specific surface area, pore volume and average fiber diameter of the TPPH$_2$-PS NFMs formed with various ratios of THF–DMF

Sample	Specific surface area (m^2 g^{-1})	Pore volume (cm^3 g^{-1})	Average fiber diameter (nm)
THF-0	2.52	0.009	951
THF-20	2.27	0.008	1933
THF-40	58.63	0.851	1609
THF-60	17.81	0.195	2807

g^{-1}, the biggest pore volume of 0.851 cm^3 g^{-1} and the smallest average fiber diameter of 1609 nm. As the low boiling point of THF content increased, the average fiber diameter of THF-60 increased while the its pore volume decreased due to the faster speed on solidification of the electrospinning jet, result to lower specific surface area. THF-0 and THF-20 have the lowest specific surface area and pore volume because of their poor porous structure in spite of their fiber diameters are small. In addition, the weight loss of the TPPH$_2$-PS NFM happens at approximately 400 °C, which confirm its good thermostability used as HCl gas sensor (Fig. S2†).

HCl gas sensing properties of the TPPH$_2$-PS NFM

The detection of HCl gas was carried out to study the sensing properties of the as-prepared TPPH$_2$-PS NFM sensor. HCl gas of certain concentration was introduced to the test chamber where the sensor was placed. The sensor samples were prepared in the same size, which the diameter is about 1 cm and the thickness is about 0.11 mm. The HCl gas exposure test was carried out at 40 °C in 50 ± 2% RH. As shown in Fig. 4, the sensor presents a visible color variation from pink to yellow green with a concentration of HCl gas up to 1000 ppm. When repeatedly flushing the protonated TPPH$_2$-PS NFM sensor with pure N$_2$ three times for 1 min, the color of the sensor is completely reverted back to its original state. This vivid color variation can be ascribed to the reversible protonation reaction between H$^+$ of HCl and the central nitrogen of the TPPH$_2$ molecule.[17,36] Initially, TPPH$_2$ molecule has a planar structure with all phenyl group perpendicular to the plane of the porphyrin ring. After protonated with HCl gas, the planarity of the porphyrin ring is destroyed and change to saddle conformation resulting to the obvious color variation of the sensor.[10,37] Considering the threshold for tolerably safe exposure to HCl gas (10 ppm) and the exposure limit in work place (5 ppm), the as-prepared TPPH$_2$-PS NFM sensor could be used to briefly evaluate the concentration of HCl gas ranging from 1 ppm to 60 ppm
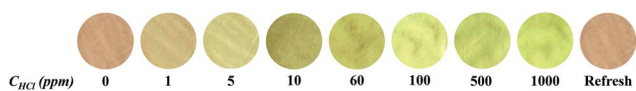

Fig. 4 Color pictures of the sample THF-40 exposed to different concentrations of HCl gas (C_{HCl}) for 30 s at 40 °C in 50 ± 2% RH and refreshed by N$_2$.

without resorting to the use of expensive instruments which is necessary for developing low-cost HCl gas sensing systems.

UV-visible absorption spectra of the TPPH$_2$-PS NFM exposed to 0–1000 ppm HCl gas are shown in Fig. 5a. It displays a distinctive Soret band around 420 nm and four weaker Q bands at 518, 552, 593 and 650 nm before HCl gas exposure. The Soret band features a gradual bathochromic shift of 22 nm, from 420 to 442 nm upon the addition of HCl gas exposed to the TPPH$_2$-PS NFM, which is consistent with the research result of Y.-Y. Lv *et al.*[24] Also the Q band at 650 nm becomes stronger as the concentration of HCl gas increases. These spectral changes are attributed to the protonation reaction between H$^+$ and the central nitrogen of the TPPH$_2$, which causes the charge-transfer complex between H$^+$ and TPPH$_2$, and hence the visible color variation of the TPPH$_2$-PS NFM.[38] As shown in Fig. 5b, fluorescence quenching is also obvious and the intensities of emission spectra at 645 nm and 710 nm decrease with the increased concentration of HCl gas which is another proof of the protonation on TPPH$_2$. When the sensor is refreshed by N$_2$, the absorption and emission spectra of the TPPH$_2$-PS NFM return to nearly the original states shown by the dash line of Fig. 5 which confirms the deprotonation of the TPPH$_2$ resulting the color recovery of the sensor.

For further study of the sensing response of TPPH$_2$-PS NFM sensor, fluorescence spectra of the sensor exposed to HCl gas with concentration of 0–3000 ppm were measured. The sensing response were calculated from specific value of the intensity at 645 nm (I_0/I). Fig. S3† shows the sensing response of the sample
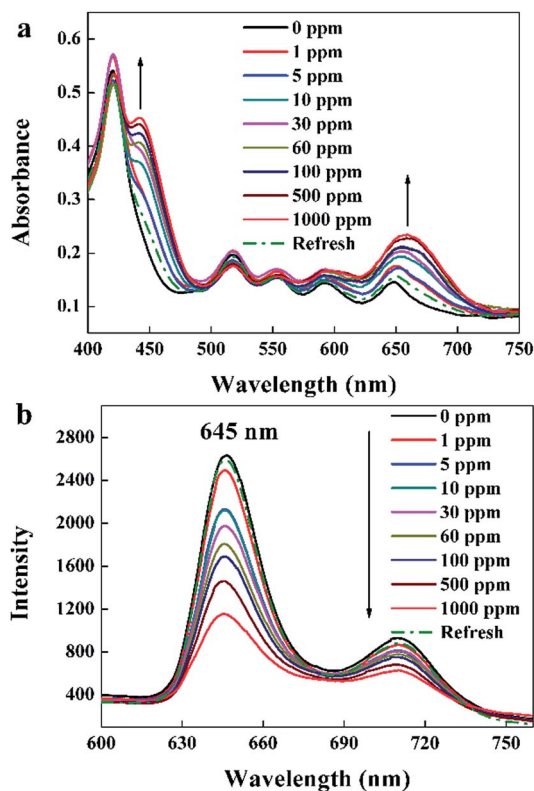
Fig. 5 UV-visible absorption spectra (a) and fluorescence spectra (b, λ_{ex} = 420 nm) of the sample THF-40 exposure to different concentrations of HCl gas for 30 s at 40 °C in 50 ± 2% RH and refreshed by N$_2$.

Paper

THF-40 exposure to different concentration of HCl gas. The slope of the curve presents a linear increase at lower HCl concentration range in 0–5 ppm. At higher concentrations, the concentration dependence conform to non-linear due to the saturation effects.[39] As shown in Fig. 6, a linear fitting is used to fit the value of I_0/I at 645 nm against the concentration of HCl gas ranging from 0 ppm to 5 ppm, which can be described by the Stern–Volmer eqn (1).[40]

$$\frac{I_0}{I} = 1 + K_{SV}[Q] \tag{1}$$

where I_0 and I represented the fluorescence intensity at 645 nm of the sensor before and after exposure to HCl gas for 30 s at 40 °C, respectively. [Q] is the concentration of HCl gas and K_{SV} is the Stern–Volmer quenching constant. The detection limit (DL) of the sensor was computed as the eqn (2).[39,41]

$$DL = \frac{3\sigma}{S} \tag{2}$$

where σ is the standard deviation of the blank signal ($n = 6$) and S is the slope of the linear calibration plot. The DL of the TPPH$_2$-PS NFM sensor toward HCl gas was found to be 46 ppb.

Fast response is a significant requirement to be considered for gas sensor. Fig. S4† shows the exposure time dependence of I_0/I at 645 nm after the sensor exposed to 100 ppm HCl gas. The slope of all the curves presents a linear increase at the initial region and turns to equilibrium after 5 s. However, the response time of compact films, such as composite film[42] and LS film,[38] based gas sensors is in several minutes which indicates that the structure of these sensing films is the major factor influencing the response time of the gas sensor. Kinetic data were fitted based on the linear region of the curves shown in Fig. S4† using kinetic models to assess the HCl gas adsorption of the TPPH$_2$-PS NFM with different structure and TPPH$_2$ content. According to eqn (1), the linear equation of pseudo-first-order and pseudo-second-order kinetics can be deformed to eqn (3) and (4).[43–46]

$$\log \frac{I_0}{I} = k_1 t \tag{3}$$

$$\frac{1}{I} = k_2 t + \frac{1}{I_0} \tag{4}$$

where I_0 and I represented the fluorescence intensity at 645 nm of the sensor before and after exposure to 100 ppm HCl gas for t s at 40 °C, respectively. k_1 and k_2 are the pseudo-first-order and pseudo-second-order rate constant. As illustrated in Table 2, the porous structure of the TPPH$_2$-PS NFM is relevant to the solvent compositions. Therefore, kinetic fitting of the TPPH$_2$-PS NFMs with various ratios of THF–DMF was shown in Fig. 7a to investigate the effect of porous structure on HCl gas adsorption. The kinetic parameters is shown in Table 3.

It is clearly indicate that the pseudo-second-order model fit the kinetic data well, with R^2 over 0.99. The sample of THF-40 has the maximum k_2 of 5.67×10^{-5} which confirm that high specific surface area and pore volume is suitable for gas adsorption and diffusion. Fig. 7b shows kinetic fitting of the TPPH$_2$-PS NFMs with different TPPH$_2$ content and the kinetic parameters of the effect of TPPH$_2$ content on HCl gas adsorption is also shown in Table 3. With the increase of the TPPH$_2$ content, the value of k_2 increases and reaches the peak with TPPH$_2$ content up to 2.0 mg mL^{-1}. As the TPPH$_2$ content further increased, the value of k_2 decreases because a large proportion of the porphyrin results in some porphyrin crystals.[42]

Reversibility, photostability and humidity insensitivity of the sensor

When the sensor is continuously monitored in rapidly alternated gaseous atmospheres, the specific value of I_0/I at 645 nm rise and recover with the environment switched between 100 ppm HCl gas and pure N$_2$ (Fig. 8a). The sensor exhibits excellent reversibility and prompt response and recovery. The response time taken as the time required to reach 90% of the steady-state value is approximately 5 s, and the recovery time taken as the time to recover the sensor to 10% of the span signal is approximately 90 s. The photostability of this sensor was measured by recording I_0/I at 645 nm per 12 h exposed to 100 ppm HCl gas and N$_2$.
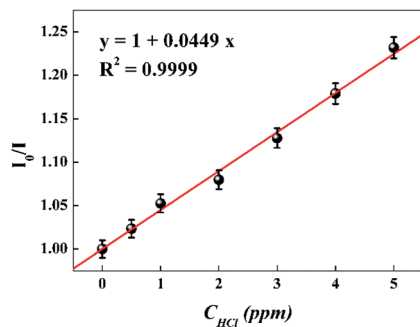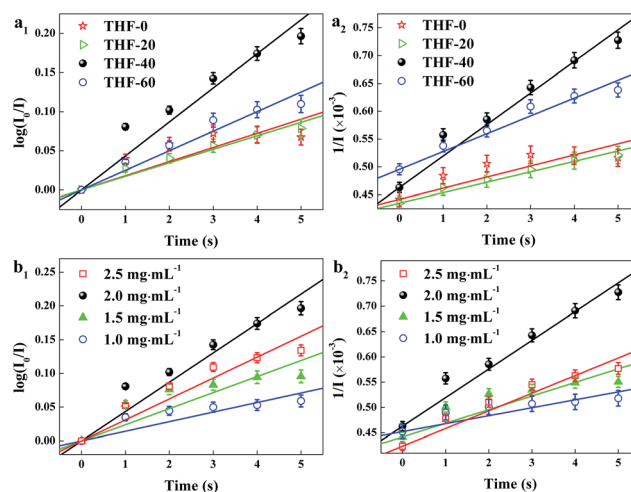

Fig. 6 Stern–Volmer plot of the sensor. I_0 and I represented the fluorescence intensity of the sensor before and after exposure to HCl gas, respectively. ($\lambda_{ex} = 420$ nm, $\lambda_{em} = 645$ nm).
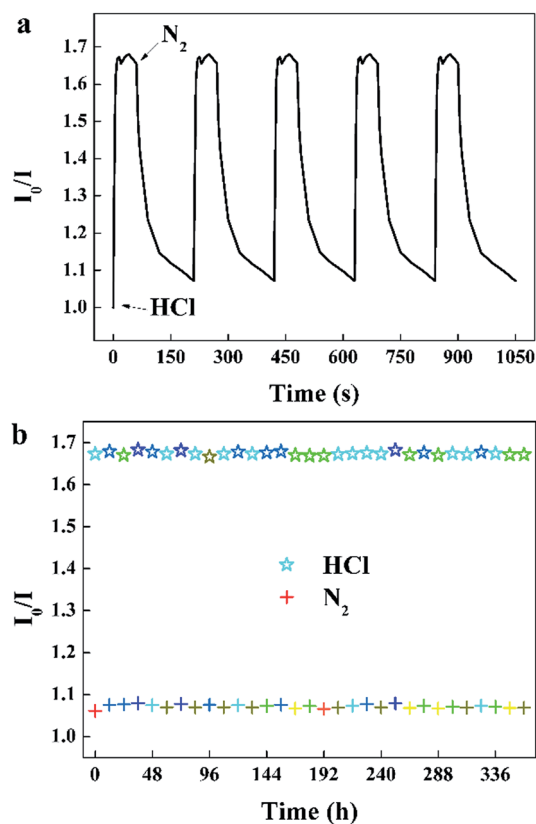

Fig. 7 Kinetic fitting of the TPPH$_2$-PS NFMs with various ratios of THF–DMF (a) and different TPPH$_2$ content (b) for the adsorption of 100 ppm HCl gas for 0–5 s. (a$_1$, b$_1$) was pseudo-first-order and (a$_2$, b$_2$) was pseudo-second-order kinetic fitting.
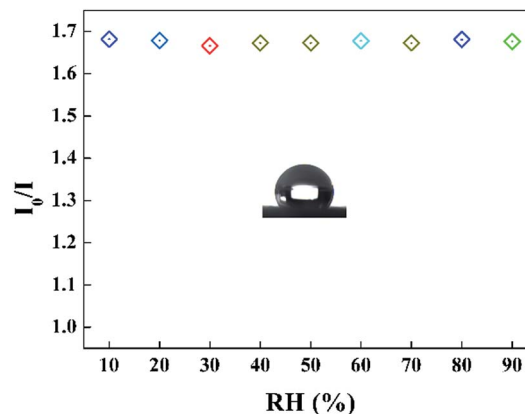
Table 3 Kinetic parameters of the effect of porous structure and $TPPH_2$ content on HCl gas adsorption

Sample	Pseudo-first-order kinetics		Pseudo-second-order kinetics	
	k_1 $(\times 10^{-2})$	R_1^2	k_2 $(\times 10^{-5})$	R_2^2
THF-0	1.81	0.890	2.00	0.998
THF-20	1.73	0.985	1.87	0.999
THF-40	4.35	0.975	5.67	0.999
THF-60	2.51	0.980	3.21	0.999
$TPPH_2$-1.0	1.42	0.911	1.57	0.999
$TPPH_2$-1.5	2.38	0.913	2.69	0.998
$TPPH_2$-2.0	4.35	0.975	5.67	0.999
$TPPH_2$-2.5	3.11	0.967	3.49	0.999

It can be seen that the sensing response of the sensor remains unchanged and the $TPPH_2$-PLA NFM shows nearly no photobleaching (Fig. 8b). In this way, the sensor can be reused many times which is important in developing low-cost HCl gas sensing systems. As shown in Fig. 9, the RH conditions have nearly no effect on sensing response of the sensor exposed to 100 ppm HCl gas in 5 s due to the hydrophobicity of the $TPPH_2$-PS NFM. The inset figure on the water contact angle of the $TPPH_2$-PLA NFM in Fig. 9 confirms its excellent hydrophobicity.

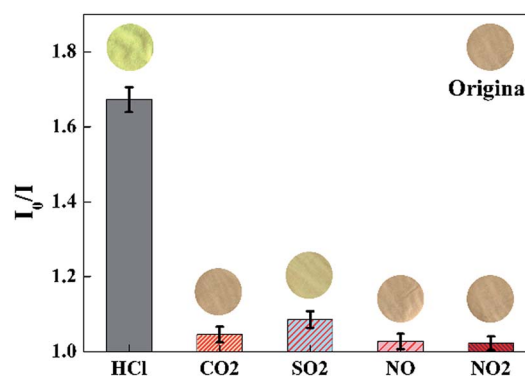Fig. 9 Sensing response of the sensor in different RH conditions (λ_{em} = 645 nm) and the inset image presents the water contact angle of the $TPPH_2$-PS NFM.

Selectivity of the sensor

To evaluate the selectivity of the proposed sensor, the sensing response (I_0/I at 645 nm) is measured in the presence of various acid gases with the concentration of 100 ppm, such as gaseous CO_2, SO_2, NO, NO_2, *etc.* As shown in Fig. 10, a significant increase of I_0/I at 645 nm could be observed when the sensor was exposed to HCl gas. By contrast, the value of I_0/I at 645 nm presented little increase when the sensor exposure to CO_2, SO_2, NO, NO_2, respectively. As shown in the inset images of Fig. 10, the color of the sensor changed from pink to yellow green exposure to HCl gas, while remained unchanged exposure to other gaseous analytes of the test.

Comparison with other HCl gas sensors based on porphyrin

The comparison of some reported porphyrin based sensors for detection of HCl gas was show in Table 4. Compared to other conventional optical sensors of HCl gas based on porphyrin, this $TPPH_2$-PS NFM sensor exhibits high sensitivity and fast response due to the large specific surface area, controllable pore sizes, well-defined porosity of the three dimensional

Fig. 8 (a) Reversibility of the sensor to alternating 100 ppm HCl gas and pure N_2, (b) photostability of the sensor exposed to 100 ppm HCl gas and N_2 for 30 s per 12 hours (λ_{em} = 645 nm).

Fig. 10 Selectivity of the sensor exposed to other acid gases with the concentration of 100 ppm for 30 s at 40 °C in 50 ± 2% RH. Inset images were the color pictures of the sensor at each gaseous analytes. (λ_{em} = 645 nm).

Table 4 Comparison with other optical sensors for detection of HCl gas based on porphyrin

Material	Method	DL (ppb)	Response time (s)	Ref.
TPPH$_2$-PS NFM	Fluorescence/colorimetric	46	5	This method
TMPyP/TiO$_2$ composite thin film	Absorbance	100	16.8 ± 0.7	47
Porphyrinated PI nanofibrous membrane	Fluorescence/colorimetric	5000	10	24
MTMP deposited glass plate	Absorbance/fluorescence	30	>180	37
TP(OH)$_4$PH$_2$ dispersed MTEOS/TEOS sol–gel film	Reflectance	500	—	18
Porphyrinated PI honeycomb film	Fluorescence	—	10	23

electrospun nanoporous fiber membrane and hence good accessibility for HCl gas. The sensor also presents good visual color change when exposure to HCl gas, which may be used for low-cost HCl sensor.

Conclusions

A fluorescent and colorimetric HCl gas sensor based on TPPH$_2$-PS NFM was facilely fabricated by electrospinning for the naked-eye detection of HCl gas. The sensor presented apparent color change from pink to yellow green when exposed to ppm-level of HCl gas at 40 °C. The sample of THF-40 showed very high sensitivity and the maximum pseudo-second-order rate constant of 5.67×10^{-5} due to its largest specific surface area and pore volume. The detection limit was found to be 46 ppb and the response time was 5 s. The sensor also showed excellent reversibility and prompt response and recovery. As this colorimetric sensing approach is simple, low-coast, sensitive and prompt, the sensor foresees a high potential for the development of visual HCl gas sensor working in smart textiles.

Acknowledgements

References

1 H. N. Kim, W. X. Ren, J. S. Kim and J. Yoon, *Chem. Soc. Rev.*, 2012, **41**, 3210–3244.

2 G. De Luca, G. Pollicino, A. Romeo and L. M. Scolaro, *Chem. Mater.*, 2006, **18**, 2005–2007.

3 M. K. LaGasse, J. M. Rankin, J. R. Askim and K. S. Suslick, *Sens. Actuators, B*, 2014, **197**, 116–122.

4 N. A. Rakow and K. S. Suslick, *Nature*, 2000, **406**, 710–713.

5 J. Sun, B. Ye, G. Xia, X. Zhao and H. Wang, *Sens. Actuators, B*, 2016, **233**, 76–82.

6 P. Kalimuthu, A. Sivanesan and S. A. John, *J. Chem. Sci.*, 2012, **124**, 1315–1325.

7 P. Muthukumar and S. A. John, *Sens. Actuators, B*, 2011, **159**, 238–244.

8 Y. Itagaki, S. Yamanaka and Y. Sadaoka, *Sens. Lett.*, 2011, **9**, 114–117.

9 K. Nakagawa, K. Kumon, C. Tsutsumi, K. Tabuchi, T. Kitagawa and Y. Sadaoka, *Sens. Actuators, B*, 2000, **65**, 138–140.

10 K. Nakagawa, Y. Sadaoka, H. Supriyatno, A. Kubo, C. Tsutsumi and K. Tabuchi, *Sens. Actuators, B*, 2001, **76**, 42–46.

11 X. C. Sun, C. Bruckner, M. P. Nieh and Y. Lei, *J. Mater. Chem. A*, 2014, **2**, 14613–14621.

12 B. P. Regmi, W. I. S. Galpothdeniya, N. Siraj, M. H. Webb, N. C. Speller and I. M. Warner, *Sens. Actuators, B*, 2015, **209**, 172–179.

13 C. Wolf, M. Tscherner and S. Kostler, *Sens. Actuators, B*, 2015, **209**, 1064–1069.

14 L. Maqueira, A. C. Valdés, A. Iribarren and C. P. de Melo, *J. Porphyrins Phthalocyanines*, 2013, **17**, 283–288.

15 P. Castillero, J. R. Sanchez-Valencia, M. Cano, J. M. Pedrosa, J. Roales, A. Barranco and A. R. Gonzalez-Elipe, *ACS Appl. Mater. Interfaces*, 2010, **2**, 712–721.

16 A. D. F. Dunbar, T. H. Richardson, J. Hutchinson and C. A. Hunter, *Sens. Actuators, B*, 2008, **128**, 468–481.

17 Y. Itagaki, K. Deki, S.-I. Nakashima and Y. Sadaoka, *Sens. Actuators, B*, 2005, **108**, 393–397.

18 Y. Itagaki, K. Deki, S.-I. Nakashima and Y. Sadaoka, *Sens. Actuators, B*, 2006, **117**, 302–307.

19 J. Spadavecchia, G. Ciccarella, P. Siciliano, S. Capone and R. Rella, *Sens. Actuators, B*, 2004, **100**, 88–93.

20 S. Jiang and M. Liu, *Chem. Mater.*, 2004, **16**, 3985–3987.

21 P. Muthukumar and S. A. John, *Sens. Actuators, B*, 2012, **174**, 74–80.

22 K. Nakagawa, T. Aono, G. Ueda, C. Tsutsumi, N. Hayase, M. Mabuchi and Y. Sadaoka, *Sens. Actuators, B*, 2005, **108**, 542–546.

23 F. W. Lin, X. L. Xu, L. S. Wan, J. Wu and Z. K. Xu, *RSC Adv.*, 2015, **5**, 30472–30477.

24 Y.-Y. Lv, J. Wu and Z.-K. Xu, *Sens. Actuators, B*, 2010, **148**, 233–239.

25 J. Lin, Y. Shang, B. Ding, J. Yang, J. Yu and S. S. Al-Deyab, *Mar. Pollut. Bull.*, 2012, **64**, 347–352.

26 M. Bognitzki, W. Czado, T. Frese, A. Schaper, M. Hellwig, M. Steinhart, A. Greiner and J. H. Wendorff, *Adv. Mater.*, 2001, **13**, 70–72.

27 R. Gentsch, B. Boysen, A. Lankenau and H. G. Borner, *Macromol. Rapid Commun.*, 2010, **31**, 59–64.

28 H. Fashandi and M. Karimi, *Polymer*, 2012, **53**, 5832–5849.

29 C. L. Casper, J. S. Stephens, N. G. Tassi, D. B. Chase and J. F. Rabolt, *Macromolecules*, 2004, **37**, 573–578.

30 S. Lu, W. Xu, Y. Chen, Y. Jiang, Q. Yao, F. Luo, Y. Wang and X. Chen, *Sens. Actuators, B*, 2016, **232**, 585–594.

31 J. Y. Lin, B. Ding, J. M. Yang, J. Y. Yu and G. Sun, *Nanoscale*, 2012, **4**, 176–182.

32 J. Lin, F. Tian, Y. Shang, F. Wang, B. Ding, J. Yu and Z. Guo, *Nanoscale*, 2013, **5**, 2745–2755.

33 J. Huang, H. Deng, D. Song and H. Xu, *Anal. Chim. Acta*, 2015, **878**, 102–108.

34 J. Lin, B. Ding, J. Yu and Y. Hsieh, *ACS Appl. Mater. Interfaces*, 2010, **2**, 521–528.

35 K. S. W. Sing, D. H. Everett, R. A. W. Haul, L. Moscou, R. A. Pierotti, J. Rouquerol and T. Siemieniewska, *Pure Appl. Chem.*, 1985, **57**, 603.

36 M. Hu, W. Kang, B. Cheng, Z. Li, Y. Zhao and L. Li, *Microchim. Acta*, 2016, **183**, 1713–1720.

37 P. Kalimuthu and S. Abraham John, *Anal. Chim. Acta*, 2008, **627**, 247–253.

38 M. Evyapan and A. D. F. Dunbar, *Sens. Actuators, B*, 2015, **206**, 74–83.

39 T. Balaji, M. Sasidharan and H. Matsunaga, *Analyst*, 2005, **130**, 1162–1167.

40 T. W. Sung and Y. L. Lo, *Sens. Actuators, B*, 2013, **188**, 702–708.

41 T. H. Richardson, C. M. Dooling, L. T. Jones and R. A. Brook, *Adv. Colloid Interface Sci.*, 2005, **116**, 81–96.

42 K. Nakagawa, K. Tanaka, T. Kitagawa and Y. Sadaoka, *J. Mater. Chem.*, 1998, **8**, 1199–1204.

43 G. R. Fonda, *J. Opt. Soc. Am.*, 1936, **26**, 316–322.

44 S. Wei, J. Liu, S. Zhang, X. Chen, Q. Liu, L. Zhu, L. Guo and X. Liu, *Hydrometallurgy*, 2016, **164**, 219–227.

45 L. J. Rather, I. Shahid ul, M. A. Khan and F. Mohammad, *J. Environ. Chem. Eng.*, 2016, **4**, 1780–1796.

46 W. Kang, X. Ma, M. Hu, Z. Jia, H. Liu and B. Cheng, *Anal. Methods*, 2016, **8**, 6489–6493.

47 M. Cano, P. Castillero, J. Roales, J. M. Pedrosa, S. Brittle, T. Richardson, A. R. González-Elipe and A. Barranco, *Sens. Actuators, B*, 2010, **150**, 764–769.